Volume 24
Number 26
14 July 2022
Pages 15607–16398

PCCP

Physical Chemistry Chemical Physics

rsc.li/pccp

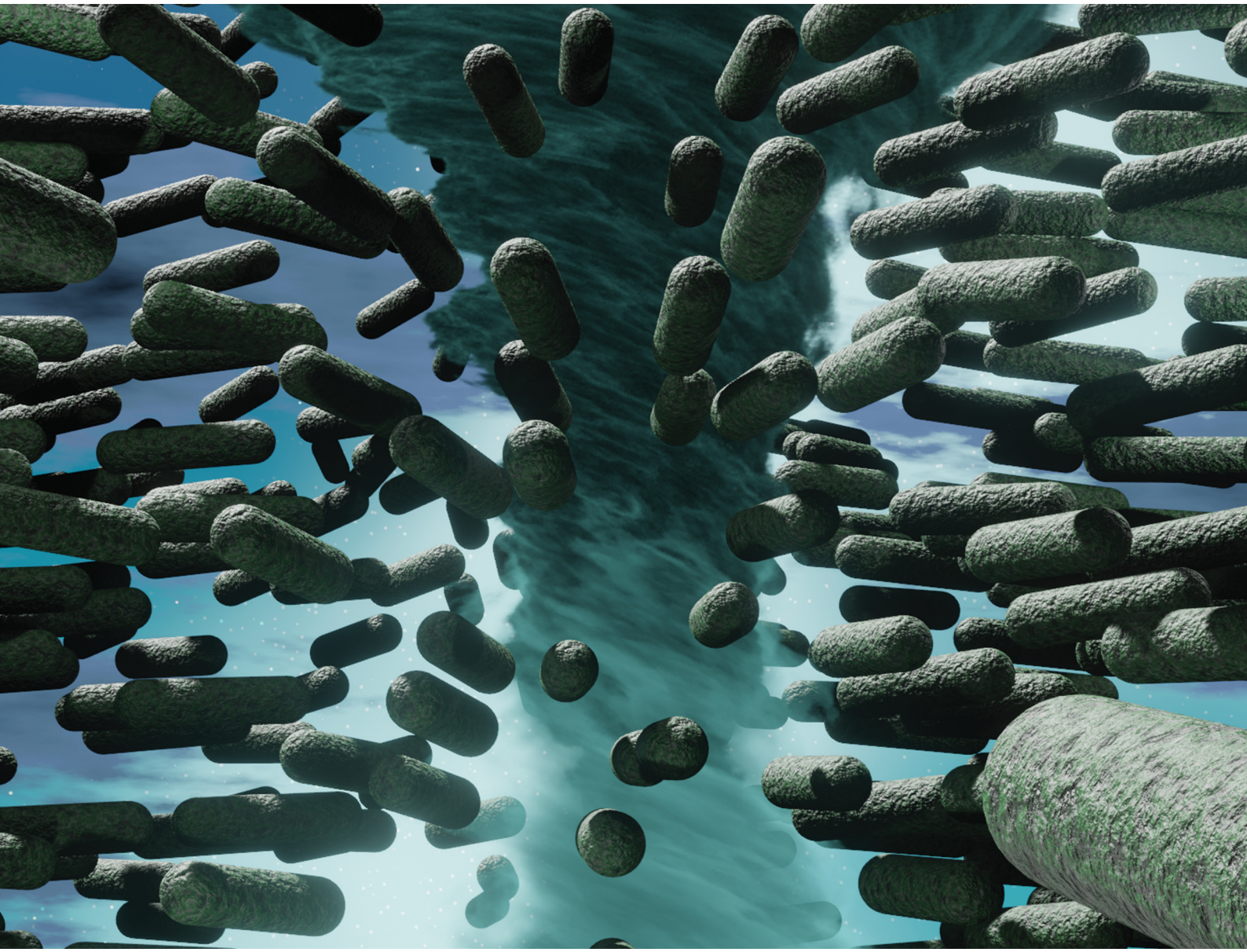

ISSN 1463-9076

ROYAL SOCIETY OF CHEMISTRY

PAPER

René Wittmann *et al.*

Topological fine structure of smectic grain boundaries and tetratic disclination lines within three-dimensional smectic liquid crystals

PCCP

ROYAL SOCIETY OF CHEMISTRY

PAPER

View Article Online
View Journal | View Issue

Cite this: *Phys. Chem. Chem. Phys.*, 2022, **24**, 15691

Topological fine structure of smectic grain boundaries and tetratic disclination lines within three-dimensional smectic liquid crystals

Paul A. Monderkamp, [a] René Wittmann, *[a] Michael te Vrugt, [b] Axel Voigt, [c] Raphael Wittkowski [b] and Hartmut Löwen [a]

Received 5th January 2022,
Accepted 26th April 2022

DOI: 10.1039/d2cp00060a

rsc.li/pccp

Observing and characterizing the complex ordering phenomena of liquid crystals subjected to external constraints constitutes an ongoing challenge for chemists and physicists alike. To elucidate the delicate balance appearing when the intrinsic positional order of smectic liquid crystals comes into play, we perform Monte-Carlo simulations of rod-like particles in a range of cavities with a cylindrical symmetry. Based on recent insights into the topology of smectic orientational grain boundaries in two dimensions, we analyze the emerging three-dimensional defect structures from the perspective of tetratic symmetry. Using an appropriate three-dimensional tetratic order parameter constructed from the Steinhardt order parameters, we show that those grain boundaries can be interpreted as a pair of tetratic disclination lines that are located on the edges of the nematic domain boundary. Thereby, we shed light on the fine structure of grain boundaries in three-dimensional confined smectics.

1 Introduction

Omnipresent throughout a vast range of chemical and physical systems,[1–12] topological defects play a central role in characterizing collective ordering phenomena. As one of the default systems for investigating such ordering phenomena, liquid crystals[13] have been enjoying continuous attention within the physical chemistry and chemical physics communities over the past decades and remain an active field of research.[14] Liquid-crystalline mesophases accompanied by topological defects occur, *e.g.*, in viral colonies,[15] bacterial DNA,[16] biopolymers,[17] and active systems[18–21] realized, *e.g.*, by swarms of bacteria[22–25] or driven filaments.[26,27] Topological analysis even provides a tool for insight into the collective behavior of animals on a macroscopic scale, *e.g.*, shoals of fish, where local coherent swimming is a vital tool in the evasion of predators.[28,29]

The most prominent type of ordering, which is typically found in liquid crystals, is orientational (nematic) ordering, where the characteristically shaped subunits, *i.e.*, molecules or colloidal particles in close proximity, show a tendency to align. This alignment can be induced or enhanced by the system boundaries.[30–32] If the nematic order gets frustrated, *e.g.*, within floating droplets,[33–37] by external confinement,[38–48] near obstacles,[49–58] or on curved surfaces,[59–65] topological defects emerge, which are discontinuities in the ordered structures that can display particle-like properties themselves.[1,20,66–68]

In liquid crystals which feature exclusively orientational order of the fluid particles, so-called nematics, the commonly observed stable defects are singular points in a two-dimensional (2d) plane and curves in three-dimensional (3d) space that are either closed or end on system boundaries. The defect strength in 2d nematic liquid crystals is characterized by a so-called topological charge, which obeys an additive conservation law in analogy to the electric charge. This topological charge is determined by the total change of the preferred local orientation of the fluid on a contour around the defects.[69,70] At higher densities and/or low temperatures, certain liquid crystals form the so-called smectic phase, which additionally displays positional order. Traditionally, the study of defects in smectic liquid crystals is mainly concerned with the purely positional defects, such as edge dislocations[71–74] or complex structures like focal conics.[75–77] However in situations, where frustration of nematic ordering takes a pronounced role, the consideration of the topology of the local orientations has proven insightful.

Smectic liquid crystals are characterized by an intrinsic layering, such that the discontinuities in the local order preferably appear as grain boundaries separating different domains within the fluid. These elongated defects possess a linear shape in two and a planar shape in three dimensions.[78]

[a] *Institut für Theoretische Physik II: Weiche Materie, Heinrich-Heine-Universität Düsseldorf, 40225 Düsseldorf, Germany. E-mail: rene.wittmann@hhu.de*
[b] *Institut für Theoretische Physik, Center for Soft Nanoscience, Westfälische Wilhelms-Universität Münster, 48149 Münster, Germany*
[c] *Institut für Wissenschaftliches Rechnen, Technische Universität Dresden, 01062 Dresden, Germany*

The formation of grain boundaries can be enforced when the fluid is confined to a container, such that the local preferred orientation in the system depends heavily on the position. This is in particular the case for colloidal liquid crystals which interact mainly through volume exclusion and possess a strong tendency to maintain a uniform layering, such that the relaxation of external constraints by elastic deformations only plays a minor role (unless favored by the confining topology).[79] For such 2d colloidal liquid crystals, we have previously elaborated that the notion of the emerging domain boundaries as topological objects with coexisting nematic and tetratic charges yields insight into the orientational topology of smectics[80] (for a comprehensive summary see Section 2.3). However, the role of the orientations within smectic liquid crystals still remains to be further understood. This concerns in particular the analysis of three-dimensional systems.

To shed more light on this issue, we present a range of simulation results for confined hard rods, representing colloidal smectic liquid crystals in three dimensions. The confinement causes frustration of the bulk symmetry and induces the formation of topological defects, which are observed and analyzed on the particle scale by treating the local orientations of the rods as indicative of the local director field. As elaborated in Section 2.3, the investigation of orientational topology in three dimensions is more involved, since 3d topological charges do not adhere to an additive charge conservation like their 2d counterparts.[69,81] However, under specific circumstances, this additive charge conservation is recovered. By elaborating on the analogy to the 2d case, we explain the effects of the introduction of the third dimension and investigate the conditions for additive topological charge conservation.

This article is structured as follows: in Section 2, we present our methodology. After elaborating in Section 2.1 on the simulation protocol, we introduce the order parameters used to characterize the simulation results in Section 2.2, while we provide a detailed discussion of the three-dimensional tetratic order parameter in Appendix A. In Section 2.3, we explain the analysis of the topological charge and the details of the charge conservation. In Section 3, we present our results, by first evaluating in Section 3.1 the order parameters to detect and classify the emerging defects in our particle-resolved snapshots. Then we characterize the layer structure and orientations within the two confinements in Section 3.2, where Appendix B provides more detailed account of the cylindrical geometry. We discuss the implications on the topological charge in Section 3.3. Lastly, we conclude in Section 4.

2 Methods

2.1 Simulations

We perform canonical Monte Carlo (MC) simulations of a model for colloidal rods confined to 3d cavities, see Fig. 1. Specifically, we consider soft walls in the shape of cylinders $\{\mathbf{r} \in \mathbb{R}^3 | r_x^2 + r_y^2 \leq R^2, 0 \leq r_z \leq h\}$ and spherical caps, resembling a drop-like shape, $\{\mathbf{r} \in \mathbb{R}^3 | r_x^2 + r_y^2 + r_z^2 < R^2, r_z > R - h\}$, both of

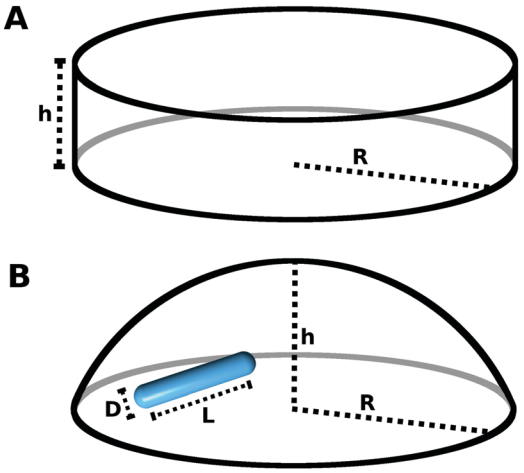

Fig. 1 Schematic depiction of the confinement considered in our simulation of three-dimensional liquid crystals. We simulate the liquid crystals by a system of N spherocylinders with length L and diameter D in confinement to suppress the bulk symmetry of the fluid in order to observe topological defects. (A) Cylindrical cavity with radius R and height h. (B) Spherical-cap cavity with radius R and height h.

radius R and height h. The rods are modeled as hard spherocylinders with aspect ratio $p = L/D = 5$, with core length L and diameter D. Note that in two dimensions, one would require significantly longer rods to observe stable smectic structures.

The pair potential for the particle–particle interaction is given by the standard hard-core repulsion[82]

$$U(\mathbf{r}_i, \mathbf{r}_j, \hat{\mathbf{u}}_i, \hat{\mathbf{u}}_j) = \begin{cases} \infty & \text{for } d_{i,j} \leq D, \\ 0 & \text{for } d_{i,j} > D \end{cases} \quad (1)$$

for spherocylinders with

$$d_{i,j} = \min_{|\alpha,\beta| < \frac{L}{2}} \left\| \mathbf{r}_i + \alpha \hat{\mathbf{u}}_i - (\mathbf{r}_j + \beta \hat{\mathbf{u}}_j) \right\|, \quad (2)$$

where $\mathbf{r}_k$ and $\hat{\mathbf{u}}_k$ are the position and normalized orientation of the k-th rod, respectively. The convexity of the confining cavities enables us to specify a wall–particle interaction potential $V(x)$ by modeling the rods as two virtual point-like particles at $\mathbf{r}_\pm = \mathbf{r}_k \pm (L/2)\mathbf{u}_k$. The interaction potential is then given by

$$V(x) = \begin{cases} \Phi(x_0) + \Phi'(x_0)(x - x_0) & \text{for } x \leq x_0, \\ \Phi(x) & \text{for } x_0 > x, \end{cases} \quad (3)$$

where $|x|$ denotes the minimal perpendicular distance from either of the two points to the wall and $x > 0$ corresponds to the inside of the cavity. The cut-off point, below which $V(x)$ is linear, is chosen as $x_0 = 0.5D$. Moreover, $\Phi(x)$ is the canonical Weeks–Chandler–Andersen-potential

$$\Phi(x) = \begin{cases} 4\varepsilon \left[\left(\frac{D}{x}\right)^{12} - \left(\frac{D}{x}\right)^{6} \right] + \varepsilon & \text{for } x \leq 2^{\frac{1}{6}} D \\ 0 & \text{for } x > 2^{\frac{1}{6}} D, \end{cases} \quad (4)$$

with $\varepsilon = 10 k_B T$ (with the Boltzmann constant k_B and the temperature T),[83] mimicking nearly hard walls. In what follows,

we consider confinements with fixed footprint radius $R = 4L$ and different heights $h \in [0.3L, 4.5L]$, whereas in Appendix B we discuss additional data for cylinder heights up to $h = 15L$.

To create the smectic structures in our 3d cavities, we follow a compression protocol, where we initialize the system at a low volume fraction $\eta_0 = 5 \times 10^{-3}$ and compress until the volume fraction $\eta_2 = 0.52$ is reached, at which the smectic-A phase is stable in the bulk. Here, the volume fraction η is defined as $\eta = NV_{\mathrm{hsc}}/V_{\mathrm{cav}}$, with the particle number N, the volume of a hard spherocylinder V_{hsc} and the total volume of the confining cavity V_{cav}. Since in each simulation run the particle geometry, the shape and size of the confinement and the final volume fraction are fixed, the particle number N is a variable that gets adjusted accordingly. The values of N we investigate, determined by the parameters above, typically lie between $N \approx 200$ for extremely shallow cavities and $N \approx 3300$ for the tallest cavities with $h = 4.5L$ that are addressed in the main part of this publication.

After initialization at $\eta_0 = 5 \times 10^{-3}$, we perform a large number of MC cycles, each of which consists of a trial displacement or rotation of each particle. The acceptance probability $P = \min\left(1, \exp\left(-\frac{\Delta U}{k_{\mathrm{B}}T}\right)\right)$ is given by the Metropolis criterion from the difference ΔU of the energies (see eqn (1) and (3)) in the system before and after trial move.[84] In detail, we compress the system for 10^6 MC cycles $\sim 10^9$ trial moves with a rate of $\Delta\eta_1 = 2.45 \times 10^{-7}$ per MC cycle to the volume fraction $\eta_1 = 0.25$ and then, in a second stage for 5×10^6 MC cycles $\sim 5 \times 10^9$ trial moves, with a rate $\Delta\eta_2 = 5.4 \times 10^{-8}$ per MC cycle to $\eta_2 = 0.52$. This two-step simulation protocol is implemented such that the majority of the simulation takes place in the regime of the packing fraction where self-assembly into the ordered phases occurs, ensuring a proper equilibration. To calculate average distribution functions and global order parameters, we gather statistics from up to 15 simulation runs.

2.2 Order parameters

We examine the structure of the confined fluid with the help of two orientational order parameters. The first one is the standard nematic order parameter $\mathcal{S}$, associated with orientational ordering of uniaxial particles, which corresponds to the largest eigenvalue of the nematic tensor $\mathcal{Q}$.[13,85] To numerically generate the scalar field $\mathcal{S}(\mathbf{r})$, we sample the nematic tensor within a spherical subsystem of radius $2.5D$ around each point $\mathbf{r}$ as

$$\mathcal{Q}(\mathbf{r}) = \left\langle \frac{3}{2}\hat{\mathbf{u}}_k \otimes \hat{\mathbf{u}}_k - \frac{1}{2}\mathbb{I}_3 \right\rangle_{B_{2.5D}(\mathbf{r})}. \tag{5}$$

Here, the brackets denote an average over all N_B particles contained within the ball $B_{2.5D}(\mathbf{r})$ with the individual orientations $\hat{\mathbf{u}}_k = (\sin\theta_k \cos\phi_k, \sin\theta_k \sin\phi_k, \cos\theta_k)^{\mathrm{T}}$ in spherical coordinates for $k \in \{1,\ldots,N_B\}$, where θ and ϕ are the angles to the z- and x-axes, respectively, and the 3d unit matrix $\mathbb{I}_3$. $\mathcal{S}(\mathbf{r})$ denotes the largest eigenvalue of $\mathcal{Q}(\mathbf{r})$. The mean local orientation $\hat{\mathbf{n}}(\mathbf{r}) = \mathbf{n}(\mathbf{r})/\|\mathbf{n}(\mathbf{r})\|$ of the rods, *i.e.*, the nematic director, can be computed by normalizing the eigenvector $\mathbf{n}(\mathbf{r})$ associated with $\mathcal{S}(\mathbf{r})$, where $\|\cdot\|$ is the Euclidean norm.

As will be discussed later, the favorable nematic bulk symmetry of orientational ordering is broken when the fluid is confined to a cavity. In two dimensions, the topological fine structure of the spatially extended defect lines in the director field $\hat{\mathbf{n}}(\mathbf{r})$ can be investigated using a scalar tetratic order-parameter field, which can be defined as

$$\mathcal{T}_{(2\mathrm{d})}(\mathbf{r}) = \left|\langle \exp(i4\phi_k)\rangle_{B_{2.5D}(\mathbf{r})}\right| \tag{6}$$

for a 2d subsystem with radius $2.5D$, with the imaginary unit i and the 2d polar angle of the k-th particle ϕ_k.[86,87] Note that this tetratic order parameter evaluates to $\mathcal{T}_{2\mathrm{d}} = 1$ when each pair of rods is either mutually parallel or perpendicular.

Similarly, in three dimensions, the discontinuities in the director field typically form grain boundaries, *e.g.*, defect planes. To develop a classification concept in three dimensions, we construct in Appendix A a 3d tetratic order parameter from the Steinhardt order parameters[88]

$$I_l = \sum_{m=-l}^{l} |\langle Y_{lm}\rangle|^2 \tag{7}$$

with the spherical harmonics Y_{lm}. Globally, this tetratic order parameter $\mathcal{T}$ is given by

$$\mathcal{T} = \frac{16\pi}{21N^2}\left|\sum_{m=-4}^{4}\left|\sum_{k=1}^{N} Y_{4m}(\theta_k,\phi_k)\right|^2 - \frac{3}{4}\sum_{m=-2}^{2}\left|\sum_{k=1}^{N} Y_{2m}(\theta_k,\phi_k)\right|^2\right|. \tag{8}$$

This definition results in $\mathcal{T} = 0$ for an isotropic system, where the orientations $\{\hat{\mathbf{u}}_k\}$ are uniformly distributed on the unit sphere S^2 and $\mathcal{T} = 1$ for a system where all orientations are pairwise either parallel or orthogonal, *i.e.*, if we have a local Cartesian coordinate system, where all rods are aligned to either of the axes. Analogously to the 2d tetratic order parameter $\mathcal{T}_{(2\mathrm{d})}$, our definition (8) of $\mathcal{T}$ implies both perfect cubatic ($\mathcal{T} = 1$, $\mathcal{S} = 0$) and perfect nematic order ($\mathcal{T} = 1$, $\mathcal{S} = 1$) as special cases of $\mathcal{T} = 1$, such that we cannot measure this kind of tetratic order in a 3d system with either the standard cubatic[89,90] or the standard nematic order parameter.

We now prove that the 3d tetratic order parameter (8) has the desired properties. First, we show that it is 0 for an isotropic system. In this case, the orientations $\{\theta_k, \phi_k\}$ approach a uniform distribution on the unit sphere S^2, such that the inner sums over k in eqn (8) approach an integral over S^2. This integral vanishes since the spherical harmonics satisfy

$$\int_{S^2} \mathrm{d}\Omega\, Y_{lm}(\theta,\phi) = 0 \tag{9}$$

for $l \neq 0$. Second, we show that it is 1 for a system where all particles are pairwise either parallel or orthogonal. Since $\mathcal{T}$ is by construction invariant under coordinate transformations and since the functions Y_{4m} and Y_{2m} are invariant under parity

transformation, we can assume without loss of generality that we have a configuration (Λ) of a particles with orientation $(\theta,\phi) = (\pi/2, 0)$, b particles with orientation $(\theta,\phi) = (\pi, 0)$ and c particles with orientation $(\theta,\phi) = (\pi/2, \pi/2)$ (with $a, b, c \in \mathbb{N}_0$). The order parameter (8) then evaluates to

$$\mathcal{T}^{(\Lambda)} = \frac{16\pi}{21(a+b+c)^2} \times \left| \sum_{m=-4}^{4} \left| a Y_{4m}\left(\frac{\pi}{2}, 0\right) + b Y_{4m}(\pi, 0) + c Y_{4m}\left(\frac{\pi}{2}, \frac{\pi}{2}\right) \right|^2 - \frac{3}{4} \sum_{m=-2}^{2} \left| a Y_{2m}\left(\frac{\pi}{2}, 0\right) + b Y_{2m}(\pi, 0) + c Y_{2m}\left(\frac{\pi}{2}, \frac{\pi}{2}\right) \right|^2 \right| = 1, \tag{10}$$

as can be easily confirmed by evaluating eqn (10) using a computer algebra system. Further examples are given in Appendix A.2.

Finally, to generate a local field $\mathcal{T}(\mathbf{r})$ of the tetratic order parameter from our simulation data, we sample the spherical harmonics entering eqn (8) only within local spherical subsystems $B_{2.5D}(\mathbf{r})$, which yields

$$\mathcal{T}(\mathbf{r}) = \frac{16\pi}{21} \left| \sum_{m=-4}^{4} \left| \langle Y_{4m}(\theta_k, \phi_k) \rangle_{B_{2.5D}(\mathbf{r})} \right|^2 - \frac{3}{4} \sum_{m=-2}^{2} \left| \langle Y_{2m}(\theta_k, \phi_k) \rangle_{B_{2.5D}(\mathbf{r})} \right|^2 \right|, \tag{11}$$

analogously to the nematic tensor, *cf.* eqn (5).

2.3 Topological charge

Topological defects are identified as discontinuities in the director field $\hat{\mathbf{n}}(\mathbf{r})$, see Fig. 2. In 2d nematic liquid crystals, the types of stable bulk defects are point defects. The strength of the defect, *i.e.*, the degree of deformation of the surrounding fluid, is typically analyzed by a topological charge Q that equates to the total rotation of the director traversing any contour $\mathcal{C}$ around the defect. This charge is given by the winding number that can be explicitly calculated as the closed line integral along the contour $\mathcal{C}$ parametrized by κ, *i.e.*,

$$Q = \frac{1}{2\pi} \oint_{\mathcal{C}(\kappa)} \left[\hat{n}_1(\kappa) \frac{\partial \hat{n}_2(\kappa)}{\partial \kappa} - \hat{n}_2(\kappa) \frac{\partial \hat{n}_1(\kappa)}{\partial \kappa} \right] \mathrm{d}\kappa, \tag{12}$$

where $\oint_{\mathcal{C}(\kappa)} \mathrm{d}\kappa = 2\pi$.[85] Due to the apolarity of the particles, the configuration space of the orientations is a semicircle with end points identified, commonly denoted by S^1/Z_2, *i.e.*, we now consider $\hat{\mathbf{n}}$ to be a headless vector in the sense that we identify $\hat{\mathbf{n}}$ and $-\hat{\mathbf{n}}$.

From a topological point of view, we define the charge *via* the winding number because (since the winding number is a discrete quantity) different contours with different winding numbers can not be continuously transformed into each other, *i.e.*, are not homotopic. All possible contours in the liquid crystal correspond to loops in S^1/Z_2. The fundamental group $\pi_1(S^1/Z_2)$ classifies loops in S^1/Z_2 up to homotopy equivalence.

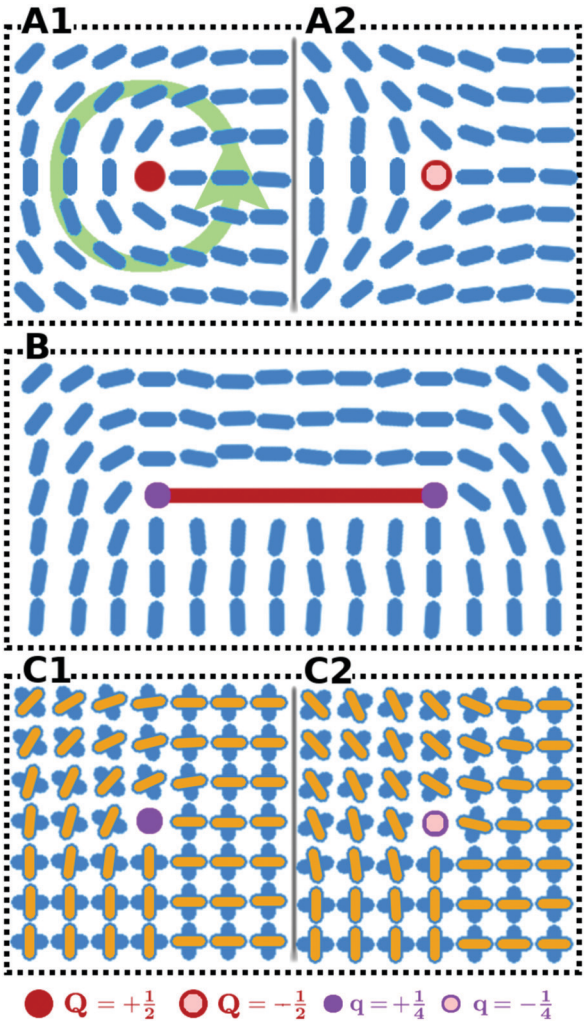

Fig. 2 Schematic of the classification of topological defects in two dimensions, present as discontinuities in the director field $\hat{\mathbf{n}}(\mathbf{r})$. The topological charge of a defect corresponds to the net rotation of $\hat{\mathbf{n}}(\mathbf{r})$ traversing the defect in counter-clockwise direction (indicated by the arrow in A1) around the defects. (A) Point defects for particles of π rotational symmetry with charges $Q = +1/2$ (A1) and $Q = -1/2$ (A2) typically present in nematic liquid crystals. (B) Decomposition of smectic grain boundaries into tetratic point defects. Due to the preferred difference in orientation angles of $\pi/2$, the line defects can be classified as two isolated tetratic point defects of charge $q = \pm 1/4$. The schematic shows an exemplary line defect of total charge $Q = q_1 + q_2 = 1/2$. (C) Point defects for particles with $\pi/2$ rotational symmetry. Charges are $q = +1/4$ (C1) and $q = -1/4$ (C2). For ease of observing the continuous rotation, the two main axes are decorated differently.

Consequently, all possible defects are classified by the fundamental group $\pi_1(S^1/Z_2)$. This group is given by $\mathbb{Z}/2$ with the addition operation +. (The prefactor 1/2 is a convention used in physics that is motivated by the geometric definition of charges *via* the winding number.) Therefore, the possible charges are $Q \in \{k/2 | k \in \mathbb{Z}\}$ and these charges can be added to find the total charge of a combination of two defects. The sum of all charges is a conserved quantity in two dimensions (since it has to match the Euler characteristic of the confinement[91]). As an example, we illustrate $Q = 1/2$ in Fig. 2A1 and $Q = -1/2$ in

Fig. 2A2. Moreover, the number of elements in $\pi_1(S^1/Z_2)$ is infinite, which is exemplified by the fact that the winding number can be any half-integer.

Defects typically observed in 3d nematics are disclination lines, along which the local orientational order is frustrated. (Point defects in three dimensions (hedgehogs) are not considered in this work.) In analogy to the 2d case, topological defects can be classified by considering closed loops in the orientational configuration space, up to homotopy equivalence. One typically analyses the defect in terms of the topology of a planar cross-section perpendicular to the disclination line.[92] Since the configuration space of the orientations in three dimensions is a hemisphere with antipodal points identified, commonly denoted by S^2/Z_2, the rotation of $\hat{\mathbf{n}}(\mathbf{r})$ along $\mathcal{C}$ forms loops in S^2/Z_2, classified by $\pi_1(S^2/Z_2)$. By rotation into the third dimension, all half-integer disclinations can be continuously mapped onto each other. Correspondingly, $\pi_1(S^2/Z_2)$ has only two elements. As a result, for instance, 3d defects with cross-sections like in Fig. 2A1 ($Q = +1/2$) and Fig. 2A2 ($Q = -1/2$) are homotopically equivalent. More specifically, the opposite charges $\pm 1/2$ correspond to opposite paths around half of the base of the hemisphere S^2/Z_2, both connecting two antipodal points. A +1/2 defect can be transformed into a $-1/2$ defect by passing the corresponding path in S^2/Z_2 over the north pole of the hemisphere. This implies that (a) the charge defined by eqn (12) is no longer a conserved quantity and (b) it can no longer be used to classify the possible configurations of the nematic liquid crystal up to homotopy equivalence. There are only two topologically distinct configurations left, namely defect and no defect. (The discussion in this paragraph and the previous paragraph follows ref. 69.)

Smectic liquid crystals, which additionally feature layering of the fluid particles, can be treated in the same spirit as nematics by considering a vector field normal to the smectic layers[93,94] or by directly working with the nematic director[95,96] (which coincides with the layer normals in the case of smectic-A order). However, if the smectic layers are sufficiently rigid, which is a prominent feature of colloidal systems, the discontinuities in the layered structure take the distinct form of elongated grain boundaries. Those grain boundaries are lines in two dimensions and planes in three dimensions. Recent insight into the orientational topology of colloidal smectics in two dimensions[80] suggests that these grain boundaries can be analyzed from the viewpoint of orientational topology by associating a topological charge to these defects as a whole. Furthermore, it has been shown that the rotation of the local director occurs mainly around the endpoints of the grain boundaries (see Fig. 2B). Those endpoints can be analyzed as isolated tetratic point defects by superimposing a tetratic director onto the fluid particles, *i.e.*, considering orientations with $\pi/2$ rotational symmetry, where one of the axis points along the main axes of the rods (see Fig. 2C). Due to the preferred difference of $\pi/2$ in the orientation angle across the grain boundary in smectics, those tetratic point defects display quarter charges $Q \in \{k/4 | k \in \mathbb{Z}\}$ (see Fig. 2C). Geometrically speaking, this is a consequence of the fact that the rotation of the director around such a defect (divided by 2π) is an integer multiple of 1/4 (and not of 1/2 as for standard nematic defects). Topologically speaking, this is a consequence of the fact that the tetratic order parameter superimposed in Fig. 2C takes values in $(S^1/Z_2)/Z_2$, which is a quarter-circle with end points identified. This order parameter becomes singular only at the endpoints, such that we can classify these endpoints as topological defects by integrating along a closed contour around them without having to pass through a singular point. The fundamental group is $\pi_1\left(\left(S^1/Z_2\right)/Z_2\right) = \mathbb{Z}/4$, where the conventional prefactor has now been set to 1/4.

An important property of smectic structures is their rigidity due to the additional constraint provided by the positional order. As will be detailed in the results in Section 3, the space occupied by the orientations $\{\hat{\mathbf{u}}_k\}$ is drastically reduced in our simulations of 3d colloidal smectic systems, *i.e.*, all orientations are approximately perpendicular close to the line disclinations. Therefore, it is no longer possible to transform the defects with $Q = +1/2$ into defects with $Q = -1/2$, implying that they are topologically distinct and that the charge Q defined by eqn (12) is effectively a conserved quantity. In this way, we construct a formalism for analyzing the 3d grain boundaries in Section 3 with the help of the previously defined 2d model.[80]

3 Results

3.1 Detection of defects *via* order parameters

Previous studies on 2d smectics in a simply-connected convex confining cavity[79,97,98] have shown the existence of a large, relatively defect-free central domain, encompassing several smectic layers, which connect opposite ends of the cavity. This bridge state can generally be observed for a large range of confinements.[80] Indeed, we find that this reference structure also persists when extending the system into the third dimension.

In our 3d study, we compare typical simulation results, shown both in Fig. 3 from a bird's eye view and in Fig. 4 using a 2d depiction, for two representative systems of hard rods confined to a cylindrical container (column 1) and spherical cap (column 2). The snapshots in Fig. 3A1 and A2 give an indication of the chosen dimensions of the confinement in terms of the dimensions of the individual particles: The height h of both cylinder and spherical cap is $2.4L$, while the diameter $2R$ of the footprint is fixed at $8L$. Both systems display what can be considered a generalized 3d bridge state. This becomes even clearer when considering the bottom view of both systems in Fig. 4A1 and A2. Apparently, the bottom layer of rods in our 3d systems forms 2d bridge states. Due to the symmetry of the cylinder, this structure is also mirrored on the top side. Even though the top surface of the spherical cap is strongly curved, the structure on it still resembles a 2d bridge state.

To study the particle orientation throughout the system in more detail, we examine the topology of the corresponding order-parameter fields. In Fig. 3B1 and B2, we visualize the data points of low nematic order by showing the regions with

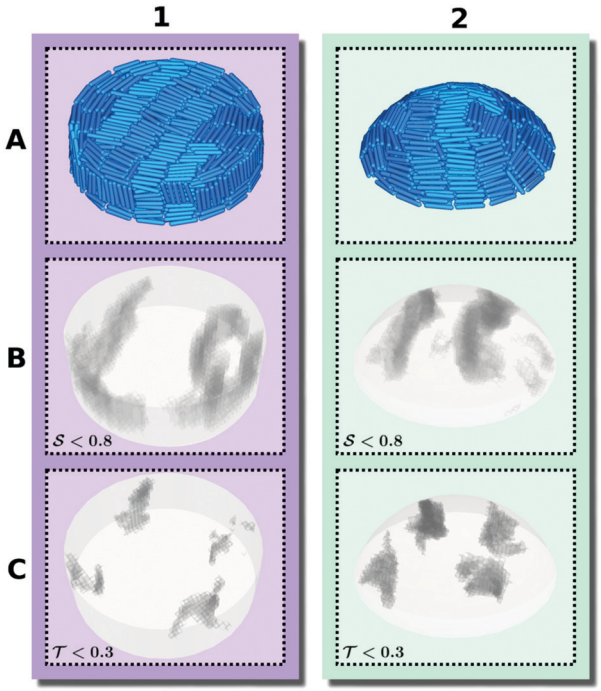

Fig. 3 Exemplary simulation results for two systems of 3d confined smectic liquid crystals. Column 1: cylinder. Column 2: spherical cap. Both systems feature height h = 2.4L and diameter 2R = 8L. Row A: Bird's eye view of the simulated system of hard rods. Row B: 3d visualization of the nematic defects according to the order parameter $\mathcal{S}(\mathbf{r})$. In order to observe the regions of low nematic order, *i.e.*, defect regions, we display the data points with $\mathcal{S}(\mathbf{r}) < 0.8$ as opaque gray clouds. Row C: 3d visualization of the tetratic defects according to the 3d tetratic order parameter $\mathcal{T}(\mathbf{r})$. To visualize the defect regions, we only display the data points with $\mathcal{T}(\mathbf{r}) < 0.3$.

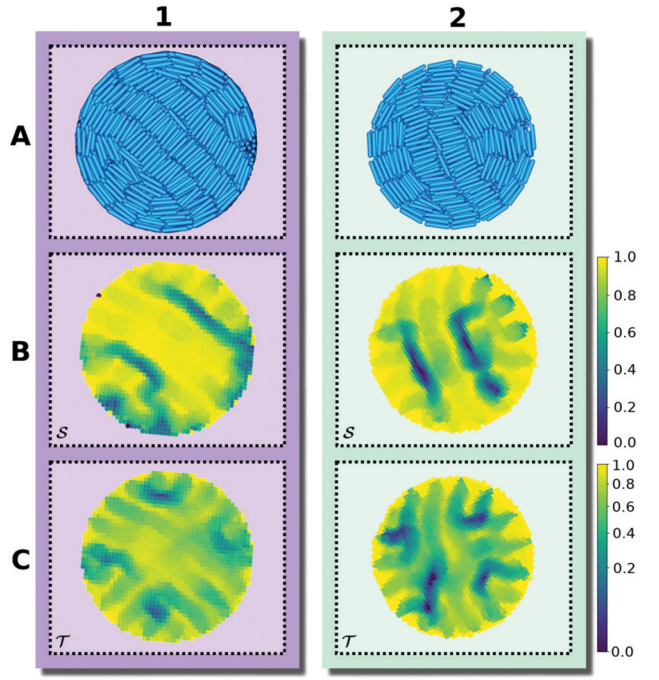

Fig. 4 The same two 3d systems as depicted in Fig. 3, but shown from a 2d perspective. Column 1: cylinder. Column 2: spherical cap. Row A: bottom view of the snapshots to exemplify the structure of the 2d cross-sections. Row B: $\mathcal{S}(\mathbf{r})$ for the system projected onto the horizontal plane. Row C: $\mathcal{T}(\mathbf{r})$ for the system projected onto the horizontal plane.

$\mathcal{S}(\mathbf{r}) < 0.8$ in gray. For both confinements, the resulting plots show a pair of planar disclinations, nestled to the sides of the central bridge domain. These defect planes reach from the top to the bottom of the container, while their shape barely varies along the vertical axis. Moreover, at cross sections of constant height, they have very little contact to the outer walls. This picture is reinforced in Fig. 4B1 and B2, which show the nematic field of the systems projected on the horizontal plane, *i.e.*, the plane perpendicular to the symmetry axis. Indeed, these projections closely resemble the nematic field $\mathcal{S}(\mathbf{r})$ for 2d systems, confirming that the shape of the defect planes varies little along the vertical axis. In addition to these grain-boundary planes, the simulated cylindrical structure gives rise to several spots where $\mathcal{S}(\mathbf{r})$ is significantly decreased at the mantle surface. As can be seen in Fig. 3A1, these spots correspond to locations where layers of single-rod depth align with the cylinder mantle. For the spherical cap, the formation of such domains is largely suppressed by the curved boundary.

Fig. 3C1 and C2 similarly show regions of low 3d tetratic order according to the order parameter $\mathcal{T}(\mathbf{r})$. In analogy to the nematic case, we locate the defects by identifying the regions where this order is minimal. Due to the relatively high sensitivity to orientational fluctuations of $\mathcal{T}(\mathbf{r})$, we display the data points only for $\mathcal{T}(\mathbf{r}) < 0.3$ in gray. It is then clearly visible that the nematic defect planes split into two tetratic defect pillars, each spanning from the bottom plane of the cavity to the top surface. Fig. 4C1 and C2 show the corresponding tetratic order-parameter field for the systems projected on the horizontal plane. This visualization shows that the minima in the order-parameter field are well localized and take an almost point-like shape. This again confirms that the tetratic disclinations in 3d appear as relatively straight lines, parallel to the vertical axis of the confinement.

In general, one identifies orientational defects as singular geometric objects in space, where the local director field $\hat{\mathbf{n}}(\mathbf{r})$ (see eqn (5)) jumps discontinuously. In particular, in 2d/3d liquid crystals with a smectic-A symmetry, the typical difference across any defect is $\pi/2$. As a result, nematic defects can be identified with the help of $\mathcal{S}(\mathbf{r})$. The same angular difference leads to a promotion of tetratic order everywhere except for the endpoints/edges, where the preferred orientation rotates. As a result, we identify a set of tetratic disclination points/lines, with the help of $\mathcal{T}(\mathbf{r})$, that sit on the endpoints/edges of each nematic defect.

3.2 Confined smectic structure

To better understand the structural details of our confined smectics, we consider the number density

$$\rho(r,z) = \frac{1}{NV_0}\sum_{k=1}^{N}\Theta\left(\frac{D}{10} - \sqrt{(z-z_k)^2 + (r-r_k)^2}\right) \qquad (13)$$

of the center positions of the rods, averaged over the azimuth, where r_k and z_k refer to the positions of the particles in

cylindrical coordinates. Here, the Heaviside step function is denoted by $\Theta(x)$ and V_0 is the intersection volume of the respective toroidal bin with the container. We further divide by the particle number N, such that $\rho(r, z)$ corresponds to the probability distribution for the position of a single particle. Additionally, we show the local orientational distribution function

$$g_2(r, z) = \langle P_2(\sin\theta_k)\rangle_{B2.5D(r,z)}, \quad (14)$$

of the rods at position (r, z), where $\sin\theta_k$ denotes the orientation of the k-th particle projected into the horizontal plane and $P_2(x)$ is the second Legendre polynomial. To obtain an appropriate resolution, we average within a spherical subsystem of radius $2.5D$.

Both quantities $\rho(r, z)$ and $g_2(r, z)$ are averaged over 15 simulations runs, with different randomized initial states. We show the resulting distribution functions in Fig. 5 for the same confinements of container height $h = 2.4L$ and diameter $2R = 8L$, presented in Section 3.1. For ease of observation, the plots are stretched in the vertical direction. We generally observe for both confinements that the density profiles distinctly show the layering structure of the fluid, reflected by the relatively localized lines close to the outside walls. This indicates, that the positions of the layers are strongly influenced by the planar surface anchoring on the outer walls. While these peaks are less pronounced further inside the cavity, the diagrams show clear indication of horizontal stacking from the bottom to the top of the confinement. We stress that the kind of layering visible in the density profiles happens on the scale of the particle diameter D and should not be confused with smectic layering along the direction of the rod axes of length $L + D$.

Along the vertical axis, the density profile for cylindrical confinement in Fig. 5A1 shows 11 layers of particles within a

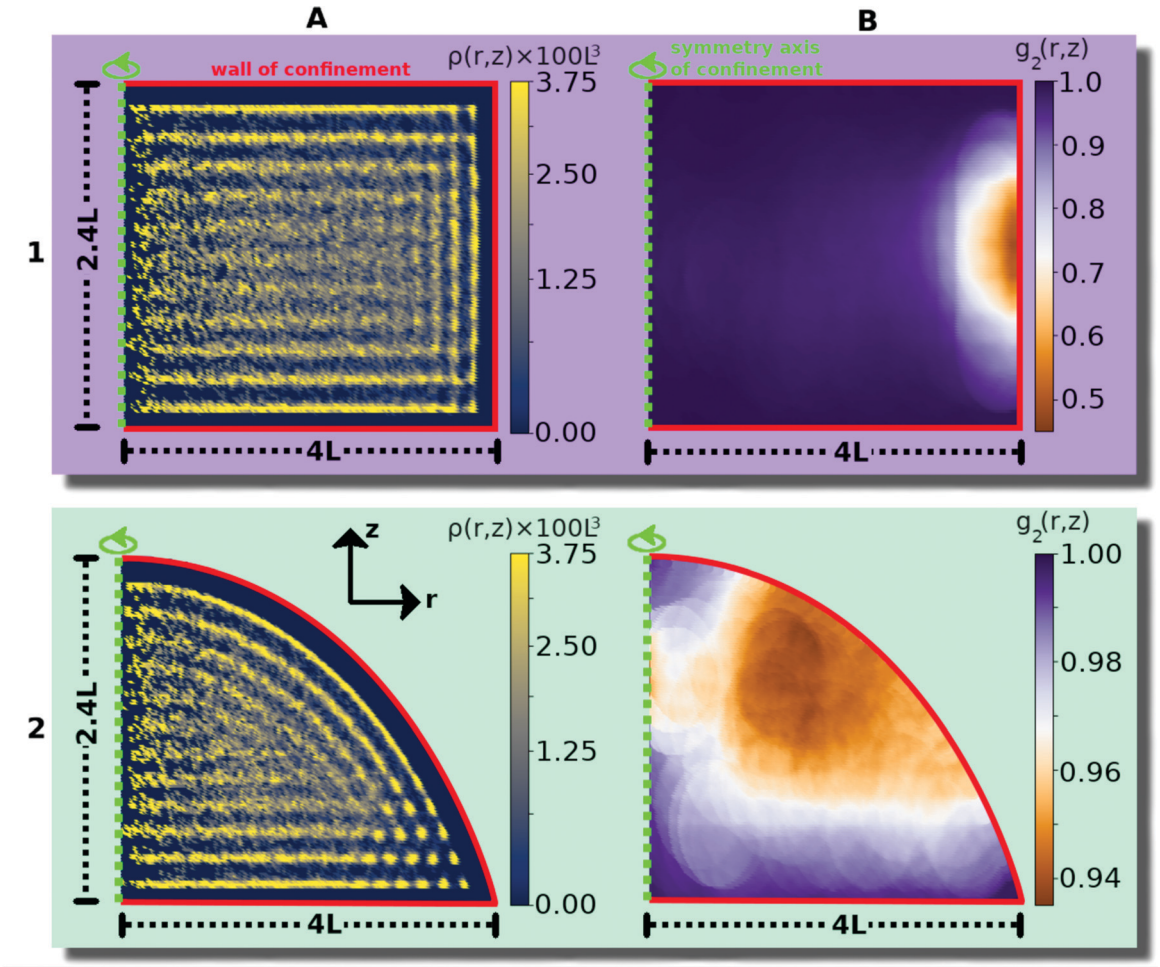

Fig. 5 Averaged structural properties of smectic liquid crystals confined in a cylinder (row 1) and spherical cap (row 2) of height $h = 2.4L$ and diameter $2R = 8L$. All diagrams are shown in cylindrical coordinates, averaged over the azimuth around the vertical center axis of the confinement (shown as a dashed green line). All diagrams are additionally averaged over 15 simulations. Column A: one-particle density $\rho(r, z)$ (defined by eqn (13)). These fields exemplify the layered fluid structure along a radial slice of the confinement, influenced by the planar surface anchoring of the confinement. To improve the contrast, we set the interval of the color bar to [0, 3.75], ensuring that the structures are clearly visible. All values above 3.75 are mapped to 3.75. Column B: correlation $g_2(r, z)$ (defined by eqn (14)) of the orientations at a certain position with the orientations projected into the horizontal plane. This function illustrates the deviation from the preferred horizontal orientation depending on the position within the confinement.

length interval of $2.4L = 12D$, indicating that their typical orientation is horizontal. This observation is reinforced in Fig. 5B1, showing that the orientations of the rods strongly correlate with the horizontal plane in almost the whole container. The depicted correlation function additionally indicates the presence of vertical rods close to the mantle of the cylinder, where $g_2(r, z)$ drops to $g_2 \approx 0.3$, consistent with the occasional appearance of vertical rods on the perimeter of the cylinder shown in the snapshot in Fig. 3A1. Accordingly, the density profile in Fig. 5A1 indicates a transition between vertical layers close to the mantle and horizontal layers in all other regions. In the corners, where the horizontal and vertical layers are compatible, we find fairly sharp isolated point-like peaks, exemplifying the high probability of a rod to sit aligned to both neighboring walls.

The density profile for the spherical-cap-shaped container in Fig. 5A2 indicates 12 stacked fluid layers in the middle of the confinement, indicating a stronger compression of the fluid than in the cylinder. Layers which are closer to the curved surface of the container are bent, while those closer to the bottom surface are horizontal. Again, we see localized peaks close to the corner, which are even more pronounced than in the cylindrical container due to the smaller opening angle. Here, the roughly 20 isolated peaks are arranged on an approximately hexagonal grid, representing the structure of rods sitting at an angle of $\pi/2$ to both walls, at approximately the same distances to the perimeter in all simulations. This clearly demonstrates the influence of the extreme confinement. Fig. 5B2 shows the orientational correlation of the rods g_2 with the bottom plane. It is visible that all rods are aligned fairly horizontally within the whole spherical cap (mind the different color scale compared to the cylindrical cavity). Only in the vicinity of the curved surface of the container, $g_2(r, z)$ is slightly reduced to values of $g_2 \approx 0.9$, indicating that the rods rotate slightly out of the horizontal plane when aligning with the curved wall.

To study the effect of confinement height h in more detail, we vary this geometrical parameter from $h = 0.3L$ to $h = 4.5L$ in steps of $0.3L$, performing in each case 15 simulations for each confining geometry. In Fig. 6, we show the resulting nematic order parameter $\mathcal{S}$ and the 3d tetratic order parameter $\mathcal{T}$ evaluated for the entire system as a function of h. For the spherical cap, both order parameters $\mathcal{S}$ and $\mathcal{T}$ globally remain at fairly constant values, irrespective of the confinement height h. In detail, the nematic order parameter settles at $\mathcal{S} \approx 0.5$, while the tetratic order parameter settles at $\mathcal{T} \approx 0.1$, only showing a slight downwards trend. In stark contrast, for cylindrical confinement the tetratic order parameter increases strongly with increasing h, while the nematic order parameter displays a nonmonotonic behavior.

Comparing the ordering behavior in the two types of cavities in more detail, we also observe in Fig. 6 that for the most shallow confinements with $h = 0.3L$ the two values of $\mathcal{T}$ are qualitatively similar, whereas $\mathcal{S}$ takes a slightly lower value in the cylinder than in the cap. For this small height of the cavities, there are practically no effects of the third dimension,

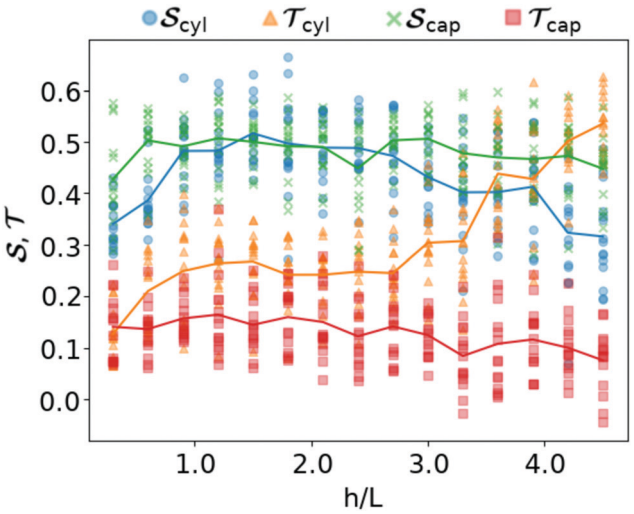

Fig. 6 Nematic order parameter $\mathcal{S}$ and tetratic order parameter $\mathcal{T}$ (see Section 2.2) for the smectic liquid crystals confined to 3d cavities in the shape of cylinders and spherical caps (see Fig. 1). Along the horizontal axis we show a range of confinements with different heights h in units of spherocylinder length L. The vertical axis represents different values of the order parameters evaluated for the entire system. For each confinement, we performed 15 simulations for each value of h. The height h is swept from $h = 0.3L$ up to $h = 4.5L$ in steps of $0.3L$. For each simulation run, we show two sets of data points, corresponding to the two order parameters $\mathcal{S}$ and $\mathcal{T}$. The curves show the order parameters averaged over the 15 simulation runs.

such that, like in a true 2d system, the aspect ratio $p = 5$ of the rods considered here is too small to result in a significant orientational order and much less a smectic bridge state. The fact that the global nematic ordering in the spherical cap is still higher than in the cylinder, relates to the decreased accessible radius of the effective circular confinement. Upon departing from this quasi-2d case by increasing h, the global order generally increases. For the cylinder, however, the nematic order parameter decreases again from $\mathcal{S} \approx 0.5$ to $\mathcal{S} \approx 0.3$, while $\mathcal{T}$ drastically increases from $\mathcal{T} \approx 0.1$ to $\mathcal{T} \approx 0.4$ as soon as $h > 1.5L$. This behavior, which is specific for the cylindrical geometry, can be explained by the fact that we observe a higher fraction of vertical rods on the mantle surface for taller confinements, reducing the global nematic order. In turn, this alignment even leads to an increase of the tetratic order, since the vertical rods are perfectly perpendicular to the central domain, such that the tetratic defects, which are exclusively formed by the horizontal rods, take a smaller percentage of the total system size. This kind of behavior is not observed for the spherical cap due to its curved boundary. For even larger cylinder heights h, the majority of rods aligns with the mantle surface such that the global nematic order increases again. This is studied in detail in Appendix B.

3.3 Topological charge

In Section 3.1, we discussed the detection of the topological defects with the help of the order parameters. As elaborated in Section 2.3, topological defects that span between system boundaries, such as those in Fig. 3 and 4, can be assigned a

topological charge defined *via* the net rotation of the director $\hat{\mathbf{n}}(\mathbf{r})$ along an encircling closed contour. More specifically, these contours can be defined within any cross section parallel to the bottom plane. Note that the sum of all topological charges, defined in this way, is a conserved quantity in 3d only under specific circumstances like in the smectic systems considered here, which can be understood as follows. Imagine, *e.g.*, that Fig. 2A1 and A2 represent cross sections of a 3d nematic system (rather than a purely 2d system). In this case, the $Q = +1/2$ defect from Fig. 2A1 can be transformed into the $Q = -1/2$ defect from Fig. 2A2 by flipping the orientations $\hat{\mathbf{u}}_k$ of all rods individually across the vertical picture axis. This transformation can be performed as a continuous mapping in 3d space, thereby obtaining a $Q = +1/2$ defect from a $Q = -1/2$ or *vice versa*. Additionally, this rotation can occur continuously along a disclination line, resulting in different values for topological charges, depending on the respective chosen cross section.[81] As a result, all possible structures can in principle be either homotopically equivalent to a charge-free structure with $Q = 0$ or to a defect structure with $Q = 1/2$.

In the previous Section 3.2, we elaborated that the confined smectic fluids in our simulations majorly consist of stacked quasi-2d layers. By showing that the 3d systems consist of a number of stacked quasi-2d layers, with no out-of-plane rotation, the defects do not undergo the transitions mentioned above. We thus argue that, in our simulations, the topological charge is equal for all horizontal cross sections, such that we can consistently define charges of any of the defects visible in Fig. 3. Additionally, we observe very similar structures on the top and bottom surface of the cylindrical systems and even on the curved surface of the spherical cap. This similarity of top and bottom structures is a further indication for a persisting structure through all horizontal slices. We can thus assume, to a good degree of approximation, that the director $\hat{\mathbf{n}}(\mathbf{r})$ does not rotate out of the 2d layers the 3d system consists of. This reduces the orientational configuration space from S^2/Z_2 to S^1/Z_2, implying that we can treat the topology in full analogy to the 2d case. In this way, by observing the bottom plane, we can infer that the total topological charge of the nematic grain boundary is equal to $Q = 1/2$ and matches the charge of the 2d counterpart. More specifically, the grain boundaries split into two pillars, *i.e.*, tetratic disclination lines, with $q = 1/4$ each, corresponding to $q = 1/4$ point charges in the cross-sections.

Less frequent exceptions to the ordering behavior described above for the considered confinements are given by the occasional alignment of the rods with the curved surface of the cap-shaped container as well as the small vertical clusters present at the mantle surface of the cylindrical container. The former case does not undergo a transition between $\pm 1/2$ charged cross sections, as no rods are present that are drastically rotated out of plane. This is supported by the fact that the flat projection of the structure on the curved surface still mirrors the structure of the bottom plane. For cylindrical cavities of comparable height, according to our observation, a director field $\hat{\mathbf{n}}(\mathbf{r})$ can most of the time be defined in a neighborhood around the defect, such that the vertical clusters do not influence the topological charges. This is in general no longer the case when the cylinder becomes sufficiently tall. As shown in Appendix B, for $h \gtrsim 5L$ full layers of vertical rods persist throughout several cross sections.

From mathematical topology it follows that for liquid crystals confined to 2d manifolds, the total topological charge in the director field has to match the Euler characteristic χ of the container.[91] The Euler characteristic χ is an algebraic invariant. Accordingly, results of previous work agree for nematic[59] as well as smectic liquid crystals[80] confined to simply-connected convex cavities and for smectics confined to 2d spherical surfaces embedded in 3d.[60] In this work, we have presented examples for 3d simply-connected convex confinements, where the sum of topological charges defined through integrating around a closed contour in a 2d cross section matches the Euler characteristic $\chi = 1$ of this cross section.

4 Conclusion

In this work, we provided an insight into the topology of defects in 3d smectic liquid crystals. In 3d smectic liquid crystals, orientational defects take the shape of extended planar grain boundaries, across which the local preferred direction jumps by an angle of $\pi/2$. Combining the established knowledge of classification of 3d nematic disclination lines with recent insights into the classification of grain boundaries as orientational defects in 2d smectic liquid crystals, we presented a formalism for the analysis of topological charge distribution. We exemplified this formalism on smectic structures in cylindrical and spherical cap containers, obtained using Monte-Carlo simulation.

In the 2d analysis one can utilize the coexistence of nematic and tetratic defects and, with the help of the tetratic order parameter, locate the points where the preferred direction rotates. Accordingly, we introduced a tetratic order parameter which can be readily applied to 3d systems. The 3d tetratic line defects were then analyzed along 2d cross sections.

In a 3d system, the sum of the winding numbers of all defects is not in general a conserved quantity since defects with different winding numbers can be transformed into each other. However, since the confined structures can be interpreted as stacked quasi-2d systems, topological charge behaves akin to electromagnetic charge and follows similar additive conservation laws. We thus found in the simulated systems that the total topological charge matches the Euler characteristic $\chi = 1$ of the containers and splits into two orientational defects, *i.e.*, two grain boundaries with topological charge $Q = 1/2$ each. Those can in turn be split into two tetratic disclination lines with charges $q = 1/4$. In general terms, we find it remarkable that the 2d topological charge, which does not have to be conserved for mathematical reasons in three dimensions, is conserved for physical reasons in the systems considered in this work.

To better understand the physical origin of the pronounced grain boundaries emerging in our confined system, let us recall that a key property of the (hard-core) colloidal system under

consideration is the rigidity of the smectic layers, such that the balance between intrinsic structure and external constraints mostly results in extended defects (grain boundaries) rather than elastic deformations. A similar observation has been made for a related 2d system using both microscopic density functional theory and colloidal experiments[79] and we expect that the same mechanism is at work in three dimensions. To get further insight, the confined systems considered in this work could therefore be investigated using density functionals for hard spherocylinders.[99,100] Alternatively, density functional theory also allows to determine elastic parameters of fluids of hard spherocylinders[101] which could then be used to fix the parameters in phenomenological elasticity theories[100,102,103] for the smectic phase.

Throughout this paper, we have in particular shed light on planar grain boundaries which split into two tetratic disclination lines. Our insight will thus be useful for the interpretation of future computational,[104,105] theoretical,[99–104,106] and experimental[79,98,107–109] research on confined smectic structures in three dimensions. To this end, our topological picture can be extended to study more complex geometries and topologies in 3d, *e.g.*, by observing $q = -1/4$ tetratic defects, which, in analogy to the 2d case, should emerge at junction points of defect networks in confinements that promote multiple domains[80] or close to concave regions of the system boundary.[79] Of interest may also be the investigation of the connection of orientational defects to positional defects, such as dislocations and focal conic domains. In nematic systems, it is widely accepted that the dynamical properties of a defect are influenced by the respective topological charge.[1,20,66–68,110] Therefore, understanding the role of smectic orientational defects, *i.e.*, grain boundaries analyzed as a connected pair of tetratic defects, in nonequilibrium is also of particular importance for understanding, *e.g.*, nucleation processes[111–114] and the dynamics[115] of smectics, as well as active liquid crystal systems,[18–21] which might also exhibit smectic order.

Conflicts of interest

There are no conflicts to declare.

Appendix A: tetratic order parameter in three dimensions

In this appendix, we provide an appropriate definition of the tetratic order parameter to characterize the topological fine structure in smectic systems of uniaxial rods.

1. Definition

In general, a system of N uniaxial particles can be microscopically described by a distribution function $f(\hat{\mathbf{u}})$ that reads

$$f(\hat{\mathbf{u}}) = \frac{1}{N}\sum_{k=1}^{N}\delta(\theta-\theta_k)\delta(\phi-\phi_k), \tag{A1}$$

where $\hat{\mathbf{u}} = (\sin\theta\cos\phi,\ \sin\theta\sin\phi,\ \cos\theta)^{\mathrm{T}}$ is the orientation vector. Such a function can be expanded as[116]

$$f(\hat{\mathbf{u}}) = \sum_{l=0}^{\infty}\sum_{i_1,\ldots,i_l=1}^{3} f^{(3\mathrm{d})}_{i_1\cdots i_l} u_{i_1}\cdots u_{i_l}, \tag{A2}$$

where u_i is the i-th element of the orientation vector and the expansion coefficients are given by[116]

$$f^{(3\mathrm{d})}_{i_1\cdots i_l} = \frac{2l+1}{4\pi}\int_{S^2}\mathrm{d}\Omega f(\hat{\mathbf{u}})\mathcal{P}^{(3\mathrm{d})}_{i_1\cdots i_l} \tag{A3}$$

with the tensor Legendre polynomials $\mathcal{P}^{(3\mathrm{d})}_{i_1\cdots i_l}$. An expansion of the form (A2) is also possible in a 2d system, in this case $\hat{\mathbf{u}}$ is a 2d vector depending on just one angle and the expression (A3) is slightly modified (see ref. 116). The second-order contribution $f^{(3\mathrm{d})}_{i_1\cdots i_2}$ is the nematic tensor. (In the main text (eqn (5)), we have, as is common, defined it with a different normalization that corresponds to multiplying the one resulting from eqn (A3) by $4\pi/5$.) An interesting mathematical property of the Cartesian expansion (A2) is that it is orderwise equivalent to the spherical multipole expansion

$$f(\theta,\phi) = \sum_{l=0}^{\infty}\sum_{m=-l}^{l} f_{lm}\,Y_{lm}(\theta,\phi) \tag{A4}$$

with the spherical harmonics Y_{lm} and the expansion coefficients

$$f_{lm} = \int_{S^2}\mathrm{d}\Omega f(\theta,\phi)\,Y^*_{lm}(\theta,\phi), \tag{A5}$$

where * denotes a complex conjugation.[116,117]

We are now looking for an order parameter that identifies configurations as ordered if the rods are either parallel or orthogonal to each other. In the 2d case, this can be simply done by superimposing tetratic order,[80] *i.e.*, fourfold rotational symmetry. Mathematically, this corresponds to measuring defects not in the nematic order-parameter field, corresponding to the second-order term in the 2d version of eqn (A2), but in the fourth-order contribution. This suggests that the desired order parameter can be constructed from the fourth-order term ($l = 4$) in eqn (A2) also in the 3d case. Since the Cartesian order parameter at fourth order has 81 components of which, due to symmetry and tracelessness, only 9 are independent, it is more convenient to work with the expansion coefficients of the angular expansion (A4) instead.

From eqn (A1) and (A5) we would then get the order parameters

$$f_{4m} = \frac{1}{N}\sum_{k=1}^{N} Y^*_{4m}(\theta_k,\phi_k) \tag{A6}$$

of order $l = 4$. The values of these order parameters (A6) depend, however, on the choice of the coordinate system. We now make use of the fact that the quantity

$$I_l = \sum_{m=-l}^{l}|\langle Y_{lm}\rangle|^2 \tag{A7}$$

with the average $\langle Y_{lm}\rangle$ is an invariant of the spherical

harmonics[88] (*i.e.*, it takes the same value for all choices of the coordinate system). This fact has been exploited in the study of bonding in liquids[88,118,119] or orientational order in liquid crystals.[120] Consequently, we should consider I_4 instead of f_{4m}.

Finally, we also need to take into account that the order parameter constructed from the invariants I_l should (a) be normalized – this can simply be ensured by multiplying it by an appropriate prefactor – and (b) not distinguish between parallel and orthogonal rods. Unfortunately, the invariant I_4 gives a larger value for parallel than for orthogonal configurations. To correct for this, we exploit the fact that the invariant I_2 measures nematic order,[120,121] such that it is large for parallel configurations. Hence, our generalized order parameter should be proportional to $I_4 - \beta I_2$, where β is a suitable prefactor. We have found an appropriate choice to be $\beta = 3/4$. Thus, we arrive at the tetratic order parameter

$$\mathcal{T} = \frac{16\pi}{21N^2}\left|\sum_{m=-4}^{4}\left|\sum_{k=1}^{N} Y_{4m}(\theta_k,\phi_k)\right|^2 - \frac{3}{4}\sum_{m=-2}^{2}\left|\sum_{k=1}^{N} Y_{2m}(\theta_k,\phi_k)\right|^2\right| \tag{A8}$$

stated in eqn (8). The prefactor ensures a proper normalization. Moreover, we use absolute values to ensure that $\mathcal{T}$ is always positive. We have tested a range of possible configurations and found that $I_4 - \beta I_2 < 0$ is measured only for isotropic systems with $|I_4 - \beta I_2| \ll 1$ (probably due to numerical fluctuations). This is reinforced by the notion that I_2 measures nematic order and systems with high nematic order result in $\mathcal{T} \approx 1$.

5.2 Examples

To get an exemplary system that should be perfectly ordered by our definition, consider three orthogonal particles with orientations $(\theta_1, \phi_1) = (\pi/2, 0)$, $(\theta_2, \phi_2) = (\pi, 0)$ and $(\theta_3, \phi_3) = (\pi/2, \pi/2)$. We find

$$\mathcal{T} = \frac{16\pi}{21\cdot 3^2}\left|\sum_{m=-4}^{4}\left|Y_{4m}\left(\frac{\pi}{2},0\right) + Y_{4m}(\pi,0) + Y_{4m}\left(\frac{\pi}{2},\frac{\pi}{2}\right)\right|^2 - \frac{3}{4}\sum_{m=-2}^{2}\left|Y_{2m}\left(\frac{\pi}{2},0\right) + Y_{2m}(\pi,0) + Y_{2m}\left(\frac{\pi}{2},\frac{\pi}{2}\right)\right|^2\right| = 1, \tag{A9}$$

as required. Similarly, for three parallel particles with orientations $(\theta_1, \phi_1) = (\theta_2, \phi_2) = (\theta_3, \phi_3) = (\pi/2, 0)$, we get

$$\mathcal{T} = \frac{16\pi}{21\cdot 3^2}\left|\sum_{m=-4}^{4}\left|3\,Y_{4m}\left(\frac{\pi}{2},0\right)\right|^2 - \frac{3}{4}\sum_{m=-2}^{2}\left|3\,Y_{2m}\left(\frac{\pi}{2},0\right)\right|^2\right| = 1. \tag{A10}$$

Finally, we flip the orientation of one particle by π to show that this leaves the order parameter invariant, implying that it is apolar. We find

$$\mathcal{T} = \frac{16\pi}{21\cdot 3^2}\left|\sum_{m=-4}^{4}\left|2\,Y_{4m}\left(\frac{\pi}{2},0\right) + Y_{4m}\left(\frac{\pi}{2},\pi\right)\right|^2 - \frac{3}{4}\sum_{m=-2}^{2}\left|2\,Y_{2m}\left(\frac{\pi}{2},0\right) + Y_{2m}\left(\frac{\pi}{2},\pi\right)\right|^2\right| = 1, \tag{A11}$$

such that eqn (A8) constitutes a solid basis for exploring tetratic order phenomena in three dimensions.

Appendix B: taller cylinders

The height h of a spherical cap is limited by the full sphere with $h = 2R$, but the respective height of a cylindrical cavity can, in principle, be chosen arbitrarily large. While in the main text, we focus on heights of the cylinder which are also possible in the cap geometry, we discuss in this appendix the behavior of the same liquid crystal systems confined to taller cylinders up to a height $h = 15L$ (*i.e.*, up to $N \approx 1.1 \times 10^4$ particles). Our results are shown in Fig. 7.

The snapshot in Fig. 7A depicts a system in a cylinder of height $h = 14L$. It is clearly visible that, along the entire mantle surface, the rods are aligned with the main axis of the cylinder. The structure at both the top and bottom layer in the cylinder (visible in the upper and lower picture, respectively, shown from the same, azimuthal viewing angle) still resembles a bridge state, which for the shorter cylindrical cavities was found to persist throughout the whole system. However, the two bridging domains have a different in-plane orientation, indicating that the structures at the top and bottom are independent.

Fig. 7B shows the orientational distribution $g_2(r, z)$ (defined by eqn (14)) sampled as average over five simulation snapshots from systems with $h = 14L$. Here, the independence of the two horizontal layers of rods at the top and bottom of the cavity becomes apparent, since throughout the majority of the system the rods are vertical. More specifically, contrasting this observation to Fig. 5B1, we notice that here the signal indicating a vertical orientation percolates throughout several horizontal slices, while for shorter cylinders the signal indicating the horizontal orientation percolates from top to bottom. Taking a closer look at the distribution for the tall cylinder, we observe that the vertical regime is slightly perturbed by horizontal stripes in the field at a distance corresponding to the smectic layer spacing. These dips correspond to the occasional occurrence of horizontal rods between the layers,[122] as is also visible in the snapshot in Fig. 7A.

Fig. 7C shows the 3d tetratic order parameter $\mathcal{T}$ as well as the standard nematic order parameter $\mathcal{S}$ (see Section 2.2) for a range $h \in [0.3L, 15L]$ of cylinder heights as an extension of Fig. 6. As the behavior for extremely shallow cavities has been discussed in detail in Section 3.2, we focus here on larger values of h. It is clearly visible from Fig. 7C that $\mathcal{S}$ has a minimum at

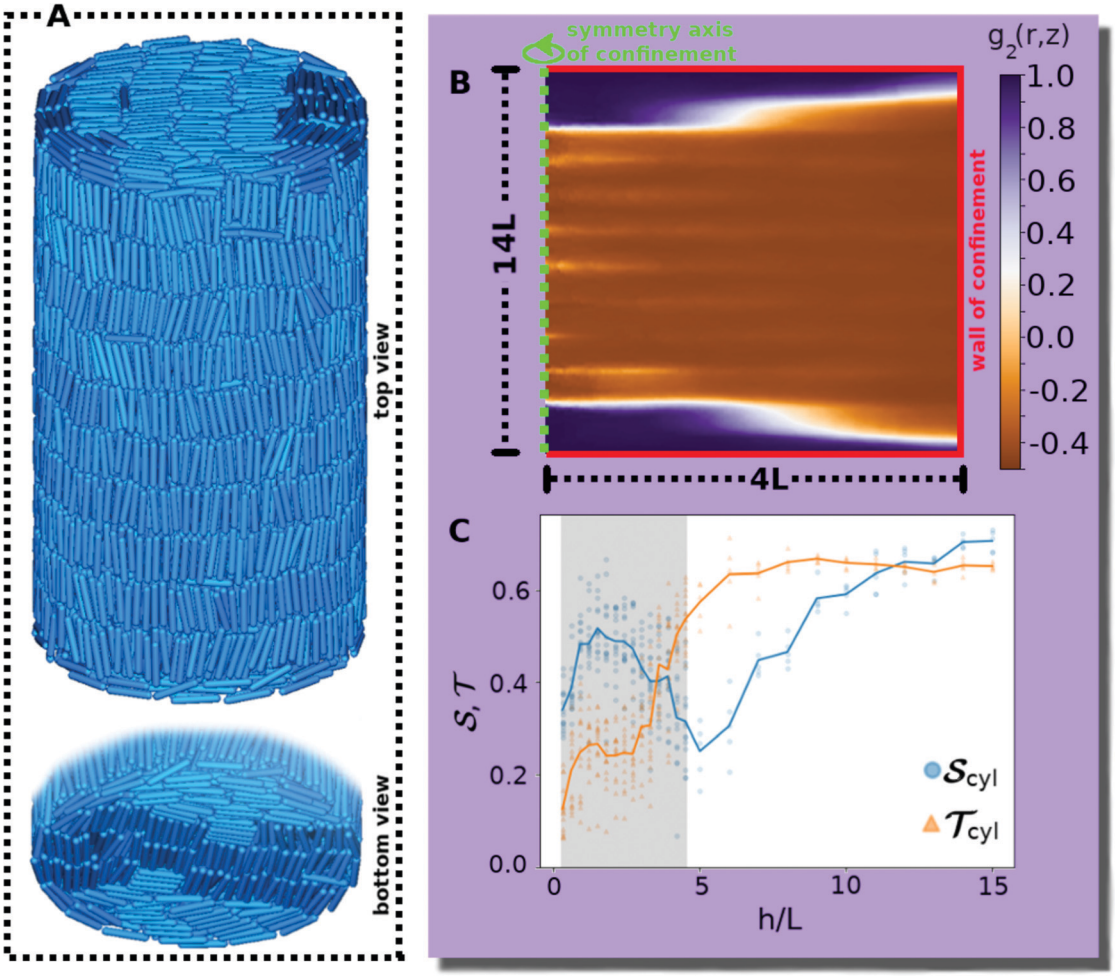

Fig. 7 Properties of smectic liquid crystals confined to cylinders of diameter $2R = 8L$ as shown in the main text but with taller heights h. (A) Representative snapshot for $h = 14L$ from a bird's eye view, as in Fig. 3A1. The picture below shows the bottom side of the same system, from the same azimuthal viewing angle. (B) Correlation function $g_2(r, z)$ (defined by eqn (14)) of the orientations at a certain position with the orientations projected into the horizontal plane for $h = 14L$, as in Fig. 5. Here, the field is generated as average over five simulation runs. (C) Nematic and tetratic order parameters $\mathcal{S}$ and $\mathcal{T}$ (see Section 2.2) with additional data for $h \in [5L, 15L]$, taken from five simulation runs. The gray background indicates the interval $h \in [0.3L, 4.5L]$ which includes the data from Fig. 6.

$h \approx 5L$, which reflects the transition from a structure with the majority of rods aligning horizontally along the top and bottom plates for short cylinders to a structure with the majority of rods aligning vertically along the cylinder mantle for tall cylinders. In the latter case, two additional grain boundaries between horizontal and vertical rods emerge close to the two ends of the cylinder, decreasing the global nematic order. When further increasing $h \gtrsim 5L$, the nematic order parameter $\mathcal{S}$ increases again until eventually reaching a plateau when the fraction of the horizontal rods and the corresponding defects become negligible. In stark contrast, the value of the tetratic order parameter $\mathcal{T}$ is not affected by the relative size of the interface between horizontal and vertical domains, such that there is no minimum around $h \approx 5L$. Instead, as soon as the vertical rods become relevant, $\mathcal{T}$ increases monotonously with increasing cylinder height h and plateaus already at $h \approx 6L$, since the tetratic defects (*cf.* Fig. 3C1) are only located in the horizontal layers.

Acknowledgements

We thank Arjun Yodh and Alice Rolf for helpful discussions. This work is funded by the Deutsche Forschungsgemeinschaft (DFG, German Research Foundation) – VO 899/19-2; WI 4170/3-1; LO 418/20-2. M. t. V. thanks the Studienstiftung des deutschen Volkes for financial support.

References

1 N. D. Mermin, *Rev. Mod. Phys.*, 1979, **51**, 591.
2 T. W.-B. Kibble, *J. Phys. A*, 1976, **9**, 1387.
3 T. Shinjo, T. Okuno, R. Hassdorf, K. Shigeto and T. Ono, *Science*, 2000, **289**, 930.
4 C. Phatak, A. K. Petford-Long and O. Heinonen, *Phys. Rev. Lett.*, 2012, **108**, 067205.
5 L. Lu, J. D. Joannopoulos and M. Soljačić, *Nat. Photonics*, 2014, **8**, 821.

6 A. Moor, A. F. Volkov and K. B. Efetov, *Phys. Rev. B*, 2014, **90**, 224512.
7 A. Tan, J. Li, A. Scholl, E. Arenholz, A. T. Young, Q. Li, C. Hwang and Z. Q. Qiu, *Phys. Rev. B*, 2016, **94**, 014433.
8 G. Yi and B. D. Youn, *Struct. Multidiscip. Optim.*, 2016, **54**, 1315.
9 A. O. Sorokin, *Phys. Rev. B*, 2017, **95**, 094408.
10 Y. Liu, Z. Wang, T. Sato, M. Hohenadler, C. Wang, W. Guo and F. F. Assaad, *Nat. Commun.*, 2019, **10**, 2658.
11 X. Lu, R. Fei, L. Zhu and L. Yang, *Nat. Commun.*, 2020, **11**, 4724.
12 C. Wang, C.-H. Chang, A. Herklotz, C. Chen, F. Ganss, U. Kentsch, D. Chen, X. Gao, Y.-J. Zeng and O. Hellwig, *et al.*, *Adv. Electron. Mater.*, 2020, **6**, 2000184.
13 P.-G. De Gennes and J. Prost, *The physics of liquid crystals*, Oxford University Press, Oxford, UK, 1993.
14 M. C. Marchetti, J.-F. Joanny, S. Ramaswamy, T. B. Liverpool, J. Prost, M. Rao and R. A. Simha, *Rev. Mod. Phys.*, 2013, **85**, 1143.
15 C. E. Fowler, W. Shenton, G. Stubbs and S. Mann, *Adv. Mater.*, 2001, **13**, 1266.
16 Z. Reich, E. J. Wachtel and A. Minsky, *Science*, 1994, **264**, 1460.
17 I. W. Hamley, *Soft Matter*, 2010, **6**, 1863.
18 L. Giomi, *Phys. Rev. X*, 2015, **5**, 031003.
19 S. J. DeCamp, G. S. Redner, A. Baskaran, M. F. Hagan and Z. Dogic, *Nat. Mater.*, 2015, **14**, 1110.
20 A. J. Tan, E. Roberts, S. A. Smith, U. A. Olvera, J. Arteaga, S. Fortini, K. A. Mitchell and L. S. Hirst, *Nat. Phys.*, 2019, **15**, 1033.
21 S. Shankar, A. Souslov, M. J. Bowick, M. C. Marchetti and V. Vitelli, 2020, arXiv:2010.00364.
22 K. Beppu, Z. Izri, J. Gohya, K. Eto, M. Ichikawa and Y. T. Maeda, *Soft Matter*, 2017, **13**, 5038.
23 A. Sokolov, I. S. Aranson, J. O. Kessler and R. E. Goldstein, *Phys. Rev. Lett.*, 2007, **98**, 158102.
24 H. H. Wensink, J. Dunkel, S. Heidenreich, K. Drescher, R. E. Goldstein, H. Löwen and J. M. Yeomans, *Proc. Natl. Acad. Sci. U. S. A.*, 2012, **109**, 14308.
25 J. Dunkel, S. Heidenreich, K. Drescher, H. H. Wensink, M. Bär and R. E. Goldstein, *Phys. Rev. Lett.*, 2013, **110**, 228102.
26 F. J. Ndlec, T. Surrey, A. C. Maggs and S. Leibler, *Nature*, 1997, **389**, 305.
27 V. Schaller, C. Weber, C. Semmrich, E. Frey and A. R. Bausch, *Nature*, 2010, **467**, 73.
28 S. J. Hall, C. S. Wardle and D. N. MacLennan, *Mar. Biol.*, 1986, **91**, 143.
29 N. Abaid and M. Porfiri, *J. R. Soc., Interface*, 2010, **7**, 1441.
30 M. Dijkstra, R. van Roij and R. Evans, *Phys. Rev. E*, 2001, **63**, 051703.
31 P. E. Brumby, H. H. Wensink, A. J. Haslam and G. Jackson, *Langmuir*, 2017, **33**, 11754.
32 E. Basurto, P. Gurin, S. Varga and G. Odriozola, *Phys. Rev. Res.*, 2020, **2**, 013356.
33 C. Chiccoli, P. Pasini, F. Semeria and C. Zannoni, *Mol. Cryst. Liq. Cryst.*, 1992, **221**, 19.
34 O. D. Lavrentovich, *Liq. Cryst.*, 1998, **24**, 117.
35 Y.-K. Kim, S. V. Shiyanovskii and O. D. Lavrentovich, *J. Condens. Matter Phys.*, 2013, **25**, 404202.
36 P. Prinsen and P. van der Schoot, *Phys. Rev. E*, 2003, **68**, 021701.
37 Y. Trukhina, S. Jungblut, P. van der Schoot and T. Schilling, *J. Chem. Phys.*, 2009, **130**, 164513.
38 Y. Trukhina and T. Schilling, *Phys. Rev. E*, 2008, **77**, 011701.
39 D. de las Heras, E. Velasco and L. Mederos, *Phys. Rev. E*, 2009, **79**, 061703.
40 O. J. Dammone, I. Zacharoudiou, R. P.-A. Dullens, J. M. Yeomans, M. P. Lettinga and D. G.-A. L. Aarts, *Phys. Rev. Lett.*, 2012, **109**, 108303.
41 O. V. Manyuhina, K. B. Lawlor, M. C. Marchetti and M. J. Bowick, *Soft Matter*, 2015, **11**, 6099.
42 A. Majumdar and A. Lewis, *Liq. Cryst.*, 2016, **43**, 2332.
43 A. H. Lewis, I. Garlea, J. Alvarado, O. J. Dammone, P. D. Howell, A. Majumdar, B. M. Mulder, M. Lettinga, G. H. Koenderink and D. G.-A. L. Aarts, *Soft Matter*, 2014, **10**, 7865.
44 I. C. Gârlea, P. Mulder, J. Alvarado, O. J. Dammone, D. G.-A. L. Aarts, M. P. Lettinga, G. H. Koenderink and B. M. Mulder, *Nat. Commun.*, 2016, **7**, 12112.
45 A. Daz-De Armas, M. Maza-Cuello, Y. Martnez-Ratón and E. Velasco, *Phys. Rev. Res.*, 2020, **2**, 033436.
46 X. Yao and J. Z.-Y. Chen, *Phys. Rev. E*, 2020, **101**, 062706.
47 X. Yao, H. Zhang and J. Z.-Y. Chen, *Phys. Rev. E*, 2018, **97**, 052707.
48 X. Yao, L. Zhang and J. Z.-Y. Chen, *Phys. Rev. E*, 2022, **105**, 044704.
49 P. Poulin, V. Cabuil and D. A. Weitz, *Phys. Rev. Lett.*, 1997, **79**, 4862.
50 R. W. Ruhwandl and E. M. Terentjev, *Phys. Rev. E*, 1997, **56**, 5561.
51 D. Andrienko, G. Germano and M. P. Allen, *Phys. Rev. E*, 2001, **63**, 041701.
52 H. Stark, *Phys. Rep.*, 2001, **351**, 387.
53 S. Čopar, T. Porenta, V. S.-R. Jampani, I. Muševič and S. Žumer, *Soft Matter*, 2012, **8**, 8595.
54 J. M. Ilnytskyi, A. Trokhymchuk and M. Schoen, *J. Chem. Phys.*, 2014, **141**, 114903.
55 S. Püschel-Schlotthauer, V. Meiwes Turrión, C. K. Hall, M. G. Mazza and M. Schoen, *Langmuir*, 2017, **33**, 2222.
56 K. Chen, O. J. Gebhardt, R. Devendra, G. Drazer, R. D. Kamien, D. H. Reich and R. L. Leheny, *Soft Matter*, 2018, **14**, 83.
57 K. H. Kil, A. Yethiraj and J. S. Kim, *Phys. Rev. E*, 2020, **101**, 032705.
58 B. Loewe and T. N. Shendruk, *New J. Phys.*, 2022, **24**, 012001.
59 J. Dzubiella, M. Schmidt and H. Löwen, *Phys. Rev. E*, 2000, **62**, 5081.
60 E. Allahyarov, A. Voigt and H. Löwen, *Soft Matter*, 2017, **13**, 8120.
61 F. C. Keber, E. Loiseau, T. Sanchez, S. J. DeCamp, L. Giomi, M. J. Bowick, M. C. Marchetti, Z. Dogic and A. R. Bausch, *Science*, 2014, **345**, 1135.

62 S. Kralj, R. Rosso and E. G. Virga, *Soft Matter*, 2011, **7**, 670.
63 I. Nitschke, M. Nestler, S. Praetorius, H. Löwen and A. Voigt, *Proc. R. Soc. A*, 2018, **474**, 20170686.
64 M. Nestler, I. Nitschke, H. Löwen and A. Voigt, *Soft Matter*, 2020, **16**, 4032.
65 I. Nitschke, S. Reuther and A. Voigt, *Proc. R. Soc. A*, 2020, **476**, 20200313.
66 A. J. Vromans and L. Giomi, *Soft Matter*, 2016, **12**, 6490.
67 K. Harth and R. Stannarius, *Front. Phys.*, 2020, **8**, 112.
68 G. Tóth, C. Denniston and J. M. Yeomans, *Phys. Rev. Lett.*, 2002, **88**, 105504.
69 G. P. Alexander, B. G.-g Chen, E. A. Matsumoto and R. D. Kamien, *Rev. Mod. Phys.*, 2012, **84**, 497.
70 M. Kléman, *Rep. Prog. Phys.*, 1989, **52**, 555.
71 R. B. Meyer, B. Stebler and S. T. Lagerwall, *Phys. Rev. Lett.*, 1978, **41**, 1393.
72 P. Chen and C.-Y. D. Lu, *J. Phys. Soc. Jpn.*, 2011, **80**, 094802.
73 C. Zhang, A. M. Grubb, A. J. Seed, P. Sampson, A. Jákli and O. D. Lavrentovich, *Phys. Rev. Lett.*, 2015, **115**, 087801.
74 R. D. Kamien and R. A. Mosna, *New J. Phys.*, 2016, **18**, 053012.
75 J. P. Bramble, S. D. Evans, J. R. Henderson, T. J. Atherton and N. J. Smith, *Liq. Cryst.*, 2007, **34**, 1137.
76 Y. H. Kim, D. K. Yoon, M.-C. Choi, H. S. Jeong, M. W. Kim, O. D. Lavrentovich and H.-T. Jung, *Langmuir*, 2009, **25**, 1685.
77 D. B. Liarte, M. Bierbaum, R. A. Mosna, R. D. Kamien and J. P. Sethna, *Phys. Rev. Lett.*, 2016, **116**, 147802.
78 M. Kléman and O. D. Lavrentovich, *Eur. Phys. J. E*, 2000, **2**, 47.
79 R. Wittmann, L. B.-G. Cortes, H. Löwen and D. G.-A. L. Aarts, *Nat. Commun.*, 2021, **12**, 623.
80 P. A. Monderkamp, R. Wittmann, L. B.-G. Cortes, D. G.-A. L. Aarts, F. Smallenburg and H. Löwen, *Phys. Rev. Lett.*, 2021, **127**, 198001.
81 S. Afghah, R. L.-B. Selinger and J. V. Selinger, *Liq. Cryst.*, 2018, **45**, 2022.
82 C. Vega and S. Lago, *Comput. Chem.*, 1994, **18**, 55.
83 H. C. Andersen, D. Chandler and J. D. Weeks, *J. Chem. Phys.*, 1972, **56**, 3812.
84 N. Metropolis, A. W. Rosenbluth, M. N. Rosenbluth, A. H. Teller and E. Teller, *J. Chem. Phys.*, 1953, **21**, 1087.
85 M. Kleman and O. D. Lavrentovich, *Soft Matter Physics – An Introduction*, Springer, New York, NY, 2003.
86 M. A. Bates and D. Frenkel, *J. Chem. Phys.*, 2000, **112**, 10034.
87 K. Zhao, C. Harrison, D. Huse, W. B. Russel and P. M. Chaikin, *Phys. Rev. E*, 2007, **76**, 040401.
88 P. J. Steinhardt, D. R. Nelson and M. Ronchetti, *Phys. Rev. B*, 1983, **28**, 784.
89 J. A.-C. Veerman and D. Frenkel, *Phys. Rev. A*, 1992, **45**, 5632.
90 P. D. Duncan, M. Dennison, A. J. Masters and M. R. Wilson, *Phys. Rev. E*, 2009, **79**, 031702.
91 M. J. Bowick and L. Giomi, *Adv. Phys.*, 2009, **58**, 449.
92 F. C. Frank, *Discuss. Faraday Soc.*, 1958, **25**, 19.
93 B. G.-g Chen, G. P. Alexander and R. D. Kamien, *Proc. Natl. Acad. Sci. U. S. A.*, 2009, **106**, 15577.
94 T. Machon, H. Aharoni, Y. Hu and R. D. Kamien, *Commun. Math. Phys.*, 2019, **372**, 525.
95 R. Pindak, C. Y. Young, R. B. Meyer and N. A. Clark, *Phys. Rev. Lett.*, 1980, **45**, 1193.
96 H.-R. Trebin, *Adv. Phys.*, 1982, **31**, 195.
97 T. Geigenfeind, S. Rosenzweig, M. Schmidt and D. de las Heras, *J. Chem. Phys.*, 2015, **142**, 174701.
98 L. B.-G. Cortes, Y. Gao, R. P.-A. Dullens and D. G.-A. L. Aarts, *J. Phys.: Condens. Matter*, 2017, **29**, 064003.
99 R. Wittmann, M. Marechal and K. Mecke, *J. Chem. Phys.*, 2014, **141**, 064103.
100 R. Wittmann, M. Marechal and K. Mecke, *J. Phys.: Condens. Matter*, 2016, **28**, 244003.
101 R. Wittmann, M. Marechal and K. Mecke, *Phys. Rev. E*, 2015, **91**, 052501.
102 J. Xia, S. MacLachlan, T. J. Atherton and P. E. Farrell, *Phys. Rev. Lett.*, 2021, **126**, 177801.
103 J. Paget, M. G. Mazza, A. J. Archer and T. N. Shendruk, 2022, arXiv:2201.09019.
104 M. Marechal, S. Dussi and M. Dijkstra, *J. Chem. Phys.*, 2017, **146**, 124905.
105 M. Chiappini, E. Grelet and M. Dijkstra, *Phys. Rev. Lett.*, 2020, **124**, 087801.
106 D. de las Heras, E. Velasco and L. Mederos, *Phys. Rev. E*, 2006, **74**, 011709.
107 W. Wang, G. Lieser and G. Wegner, *Liq. Cryst.*, 1993, **15**, 1.
108 T. Lopez-Leon, A. Fernandez-Nieves, M. Nobili and C. Blanc, *J. Phys.: Condens. Matter*, 2012, **24**, 284122.
109 A. Repula and E. Grelet, *Phys. Rev. Lett.*, 2018, **121**, 097801.
110 G. P. Crawford and S. Zumer, *Liquid crystals in complex geometries: formed by polymer and porous networks*, CRC Press, Boca Raton, Florida, USA, 1996.
111 H. Maeda and Y. Maeda, *Phys. Rev. Lett.*, 2003, **90**, 018303.
112 T. Schilling and D. Frenkel, *Phys. Rev. Lett.*, 2004, **92**, 085505.
113 R. Ni, S. Belli, R. van Roij and M. Dijkstra, *Phys. Rev. Lett.*, 2010, **105**, 088302.
114 A. Cuetos, E. Sanz and M. Dijkstra, *Faraday Discuss.*, 2010, **144**, 253.
115 E. Grelet, M. P. Lettinga, M. Bier, R. van Roij and P. van der Schoot, *J. Phys.: Condens. Matter*, 2008, **20**, 494213.
116 M. te Vrugt and R. Wittkowski, *AIP Adv.*, 2020, **10**, 035106.
117 M. te Vrugt and R. Wittkowski, *Ann. Phys.*, 2020, **532**, 2000266.
118 W. Lechner and C. Dellago, *J. Chem. Phys.*, 2008, **129**, 114707.
119 H. Tanaka, *Eur. Phys. J. E*, 2012, **35**, 113.
120 B. S. John, C. Juhlin and F. A. Escobedo, *J. Chem. Phys.*, 2008, **128**, 044909.
121 R. Blaak, D. Frenkel and B. M. Mulder, *J. Chem. Phys.*, 1999, **110**, 11652.
122 R. van Roij, P. Bolhuis, B. Mulder and D. Frenkel, *Phys. Rev. E*, 1995, **52**, R1277.

